ACS OMEGA

http://pubs.acs.org/journal/acsodf

Article

Vivianite and Its Oxidation Products in Mammoth Ivory and Their Implications to the Burial Process

Mengmeng Shen, Zhiyun Lu, Yan Xu, and Xuemei He*

Cite This: *ACS Omega* 2021, 6, 22284−22291

Read Online

ACCESS | Metrics & More | Article Recommendations

ABSTRACT: The phase composition and distribution characteristics have been obtained from two mammoth ivory samples with typical blue and yellowish-brown outer layers. The results reveal that hydroxyapatite, newberyite, organic matter, and quartz exist in all structures of mammoth ivory. Vivianite and santabarbaraite mainly contribute to the blue and yellowish-brown oxide layers of mammoth ivory, respectively. Meanwhile, metavivianite also occurs and partly influences the appearance of oxide layers. Vivianite is a common and complex product that can be formed by the interaction of gradually infiltrated Fe^{2+} and the original PO_4^{3-} in mammoth ivory. At the later stage, vivianite can be oxidized into metavivianite and santabarbaraite. As a result, mammoth tusks present dark bluish-green and yellowish-brown appearances. The multi-colored oxide layers are formed by different contents of vivianite and its oxidation products, which also provides valuable information on the relative burial intensity and time in different structures. It is inferred that the burial intensity increases in the sequence of yellowish-white dentin → blue outer layer → yellowish-brown outer layer. These observations are hopeful to be widely used in evaluating the changeable burial environment and exploring historical events that occurred on mammoth ivory.

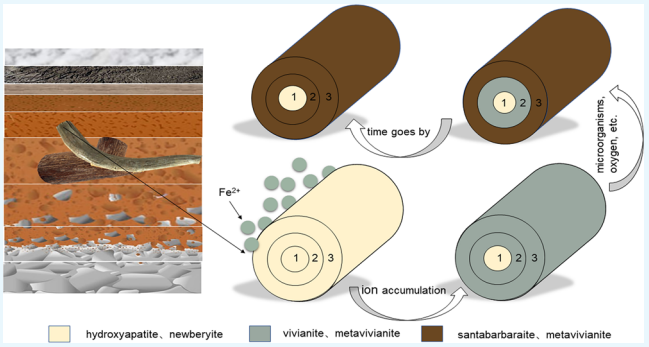

INTRODUCTION

In paleontology and archeology, researchers have observed the chemical composition and physical characteristics of mammoth ivory to obtain information about environmental evolution in the Upper Paleolithic.[1−8] Based on the symbolic ancient mammoth ivory tools and artifacts, the origin and evolution of ancient technologies and cultural differences of different communities were identified.[9−14] The woolly mammoth is an extinct species of the Elephantidae with its tusks mostly buried in ice sheets or frozen soil in the northern hemisphere.[15] The curved mammoth tusks generally present a light yellow to white color with a yellowish-brown surface darkened by burial.[16,17] With the wide application of mammoth ivory in gemology, its mineral composition is gradually understood by researchers. The dentin of mammoth tusks is composed of hydroxyapatite ($Ca_5(PO_4)_3(OH)$), newberyite ($MgHPO_4 \cdot 3H_2O$), organic matters, and other minerals.[18,19] After the outer layer of tusks became yellowish brown by burial, the crystallinity of hydroxyapatite increased, and the organic components partly lost, which can reflect the mineralization degree of mammoth ivory.[18,20,21] Recently, the disseminated blue substances have been found on the surface of unearthed mammoth ivory.[22] However, their mineral and chemical composition characteristics have not been reported in detail. In this paper, two typical mammoth ivory samples from Yakutsk, Russia, were taken as the research objects. Each mammoth ivory contains yellowish-white, blue, and yellowish-brown regions (Figure 1a). The mineralogy, chemical composition characteristics, and their influence on the appearance of representative mammoth ivory samples were investigated by petrography, spectroscopy, and chemical composition analyses. The results provide evidence to indicate the burial diagenetic processes in the blue and yellowish-brown outer layers of mammoth ivory.

MATERIALS AND METHODS

Eleven mammoth ivory samples with the yellowish-white dentin and blue and yellowish-brown outer layers were unearthed from the permafrost in Yakutsk, Russia, by Wannian Jixiang (Beijing) Jewelry Co., Ltd. Two representative polished samples, i.e., cross section and longitudinal section, were selected as the experimental samples in this paper, numbered MI-1 and MI-2, respectively. The transition layer between the yellowish-white dentin and yellowish-brown outer layer

Received: June 6, 2021
Accepted: August 3, 2021
Published: August 17, 2021

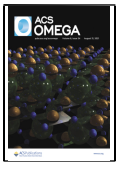

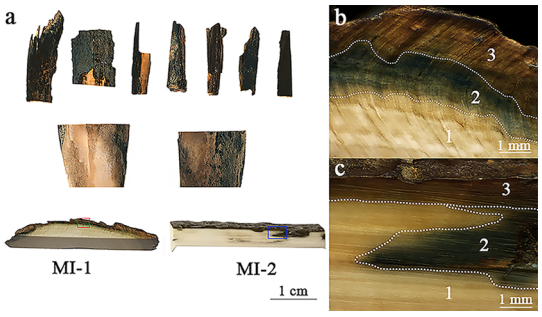

Figure 1. Appearances of mammoth ivory samples from Yakutsk, Russia. (a) Eleven mammoth ivory samples with the yellowish-white dentin (1), blue outer layer (2), and yellowish-brown outer layer (3). (b,c) Details of the red rectangle region in MI-1 and blue rectangle region in MI-2.

presents blue and bluish-green appearances. To describe this transition layer more conveniently, it is represented by the blue outer layer because the blue color is the most representative.

The scraps of the yellowish-white dentin and blue and yellowish-brown outer layers were separately pulverized to 300 mesh powders for powder X-ray diffraction (XRD) analysis. The powder XRD data were collected with a Rigaku D/Max-RC diffractometer. The instrument was equipped with a conventional copper target X-ray tube set to 40 kV and 200 mA and a graphite monochromator. The scanning speed was 7.2°/min in the test range of $3° < 2\theta < 70°$. The data were processed by using the Search-Match software package with the International Center of Diffraction Data (ICDD).

The infrared spectra (IR) of the yellowish-white dentin and blue and yellowish-brown outer layers were collected using a Tensor 27 Fourier infrared spectrometer. The acquisition was set at 32 scans in the range of 4000−400 cm^{-1}. The resolution was 2 cm^{-1}. KBr compression and transmission modes were used in the experiment.

A HORIBA HR-Evolution Raman spectrometer was adopted to measure the Raman spectra for the different color regions of MI-1 under the conditions of 50× magnification objectives and 50−1250 cm^{-1} test range. The system was equipped with 532 and 785 nm solid stage lasers. The acquisition time was 20 s, the accumulation was 3 scans, and the minimum pixel was 1 cm^{-1}.

The elemental maps of MI-1 and MI-2 were obtained using a Bruker Micro-XRF spectrometer (M4 TORNADO). The spectrometer was equipped with an X-ray tube (Rh anode) with polycapillary X-ray optics. The system worked at 50 kV and 599 μA, with chambering in air at 1.5 mbar and an acquisition time of 10 ms per pixel. The data were processed by the mineral analyzer software for M4 TORNADO.

The O (1s), P (2p), and Fe (2p) spectra of the yellowish-white dentin and blue and yellowish-brown outer layer powder

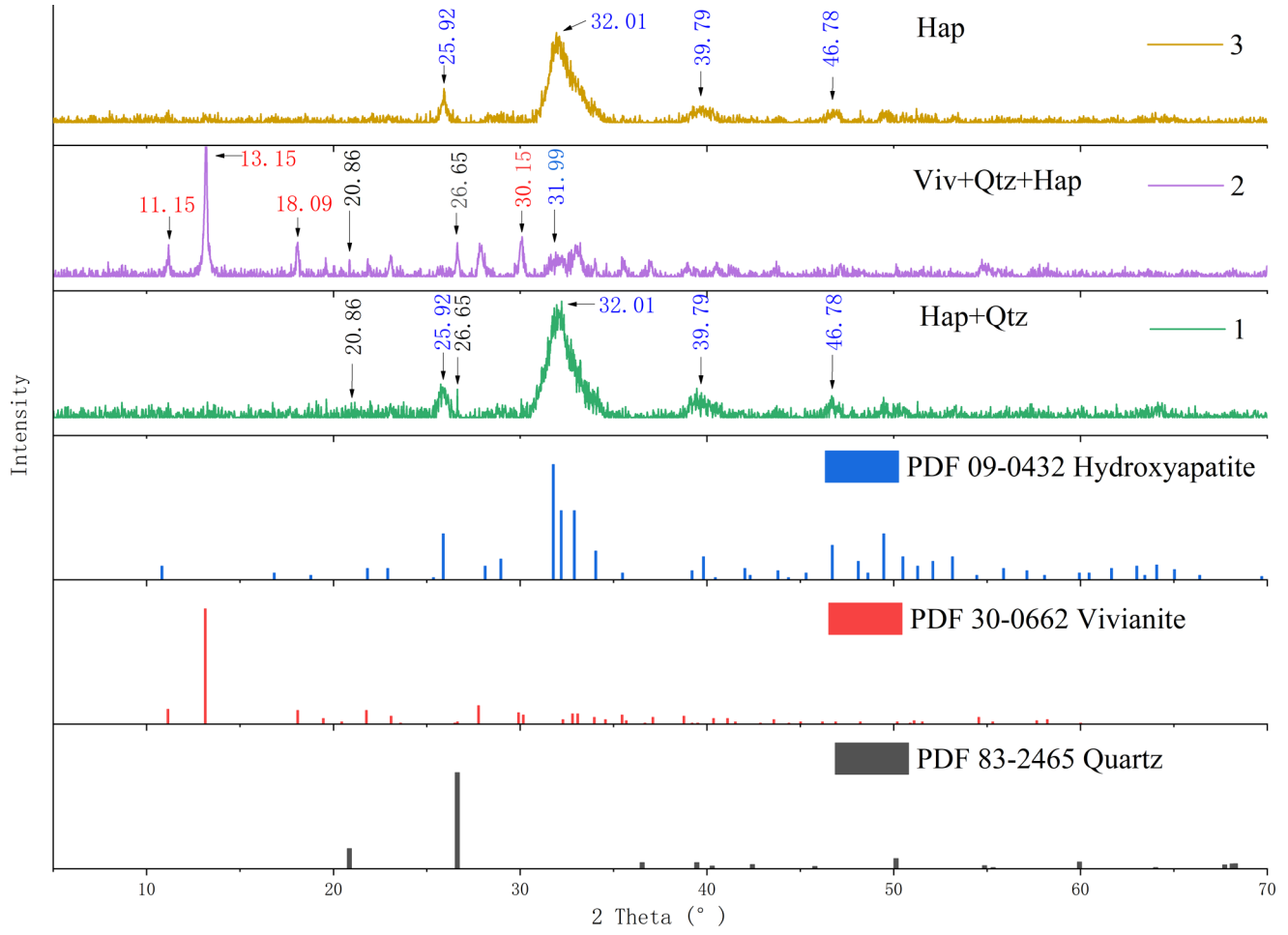

Figure 2. Powder XRD patterns of the yellowish-white dentin (1), blue outer layer (2), and yellowish-brown outer layer (3) in MI-1. Hap, hydroxyapatite. Viv, vivianite. Qtz, quartz.

https://doi.org/10.1021/acsomega.1c02964
ACS Omega 2021, 6, 22284−22291

samples were acquired using a Thermo Fisher Scientific Escalab 250Xi spectrometer configured with the 650 μm square test regions and an Al Kα radiation source (photon energy 1486.6 eV). The C (1s) peak (284.6 eV) was used to calibrate the position of binding energy. The equipment worked at a vacuum of 1×10^{-9} mbar and a constant energy of 50 eV. The CasaXPS software, Shirley background, and Gaussian:Lorentz function = 60:40 were used to fit the XPS data.

RESULTS

XRD. In this paper, the representative sample MI-1 was selected for the XRD test. The powder XRD data for three regions of MI-1 are shown in Figure 2. Mammoth ivory is mainly composed of amorphous hydroxyapatite and organic matter, so the obtained spectra present an unavoidable noise. Four strong peaks at d = 3.43 Å (2θ = 25.92°), 2.79 Å (2θ = 32.01°), 2.26 Å (2θ = 39.79°), and 1.94 Å (2θ = 46.78°) for the yellowish-white dentin and yellowish-brown outer layer of MI-1 are consistent with the characteristic diffraction peaks of hydroxyapatite (ICDD PDF 09-0432) in the crystal planes of (002), (211), (310), and (222). The large bulge-like diffraction peak between 30.00 and 35.00° appeared in these two regions, indicating the existence of amorphous hydroxyapatite.[22] There are four characteristic peaks at d = 7.93 Å (2θ = 11.15°), 6.73 Å (2θ = 13.15°), 4.90 Å (2θ = 18.09°), and 2.96 Å (2θ = 30.15°), corresponding to vivianite ($Fe^{2+}{}_3(PO_4)_2 \cdot 8H_2O$) (ICDD PDF 30-0662) in the (110), (020), (200), and (211) crystal planes, respectively. An additional weak diffraction peak at $d_{(211)}$ = 2.80 Å (2θ = 31.99°) is attributed to hydroxyapatite. It indicates that the blue outer layer of MI-1 is mainly composed of vivianite and smaller amounts of hydroxyapatite. There are two other peaks at $d_{(100)}$ = 4.25 Å (2θ = 20.86°) and $d_{(101)}$ = 3.34 Å (2θ = 26.65°) for the yellowish-white dentin and blue outer layer of MI-1. These peaks are consistent with the data for quartz (SiO_2) (ICDD PDF 83-2465), showing that quartz exists in both regions.

Microscopic Observation. The developed fissures and irregular curves are presented on the rough and dry surface of MI-1 (Figure 3a). The blue, bluish-green vivianite and other substances are exposed after the loosely structured yellowish-brown outer layer was shed (Figure 3a). The colors of the cross section from inside to outside are yellowish-white, blue and bluish-green, and yellowish-brown in that sequence (Figure 3b). The dentin is light yellow to white, with a roughly parallel wavy texture. Vivianite and other substances invade the dentin in a point distribution. They are mostly concentrated in the blue outer layer or the gaps connected with the external environment. The yellowish-brown outer layer of mammoth tusks continuously and uniformly form external to internal spreads (Figure 3b).

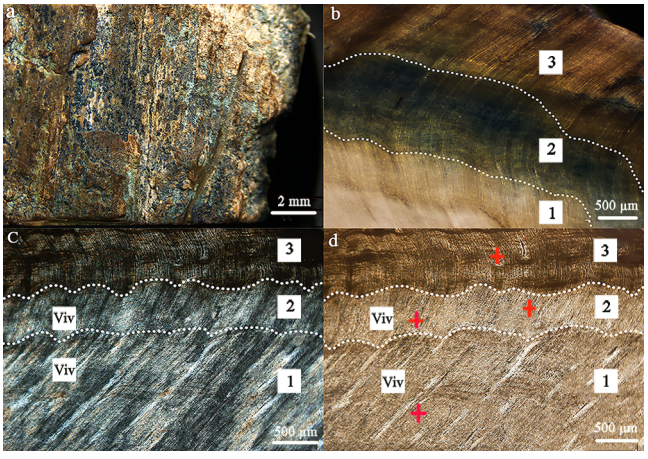

Figure 3. Microscopy images of MI-1: (a) surface. (b) Cross section with the yellowish-white dentin (1), blue outer layer (2), and yellowish-brown outer layer (3). (c,d) MI-1 thin-section under CPL and PPL. Cross symbols label the Raman test locations.

In the above three regions, the local fibrous structural units are the first-order (1st) dark gray interference color and parallel extinction under cross-polarized light (CPL). They are deduced to be hydroxyapatite (Figure 3c).[23,24] Vivianite presents the 1st yellowish-white interference color and an obvious pleochroism of blue (Np)-colorless (Nm)-light brown (Ng) under CPL.[25] In addition, it shows the moderate relief under plane-polarized light (PPL) (Figure 3d).[26] The results show that vivianite is mainly distributed in the blue outer layer, and it is also found in the yellowish-white dentin (Figure 3c,d). Quartz cannot be accurately identified under a polarizing microscope because of its low content and similar interference color with hydroxyapatite.

Infrared Spectra. The IR spectra of the yellowish-white dentin and blue and yellowish-brown outer layers of MI-1 are shown in Figure 4. In the three IR spectra, a band at around

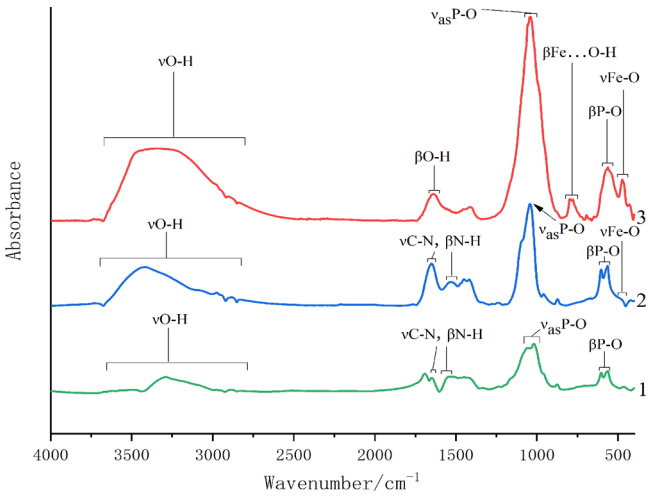

Figure 4. Infrared spectra of the yellowish-white dentin (1), blue outer layer (2), and yellowish-brown outer layer (3) in MI-1.

3250 cm^{-1} is observed. It is attributed to the O−H stretching vibration, which is associated with the adsorbed water, vivianite, and its oxidation products.[27] The peak at 1450 cm^{-1} and the overlapping band centered at 1000 cm^{-1} are due to the P−O symmetric and antisymmetric stretching modes in each spectrum, respectively.[28] Furthermore, the three IR spectra all exhibit the P−O shear bending components at 560 cm^{-1}.[29]

The peaks at 1650 and 1538 cm^{-1} separately appear for spectra 1 and 2, which are both caused by the N−H bending vibration and C−N stretching vibration of amide.[28] The shoulder peak at 475 cm^{-1} for spectrum 2 is associated with the Fe−O stretching vibration. Meanwhile, the peaks at 777 and 475 cm^{-1} of spectrum 3 are attributed to the Fe···O−H vibration and Fe−O vibration, respectively.[30] These peaks demonstrate that iron phosphate exists in the blue, yellowish-

https://doi.org/10.1021/acsomega.1c02964
ACS Omega 2021, 6, 22284−22291

brown outer layers. The presence of metavivianite ($Fe^{2+}Fe^{3+}{}_2(PO_4)_2(OH)_2{\cdot}6H_2O$) in the yellowish-brown outer layer is indicated by the Fe···O−H bending vibration at 777 cm^{-1}.[31] In addition, the band near 1635 cm^{-1} is attributed to the bending vibration of the adsorbed water, proving that the yellowish-brown outer layer contains santabarbaraite ($Fe^{3+}{}_3(PO_4)_2(OH)_3{\cdot}5H_2O$).[32]

Raman Spectra. The Raman spectra recorded for the yellowish-white dentin, blue outer layer, and yellowish-brown outer layer of MI-1 are shown in Figure 5. In each of the four

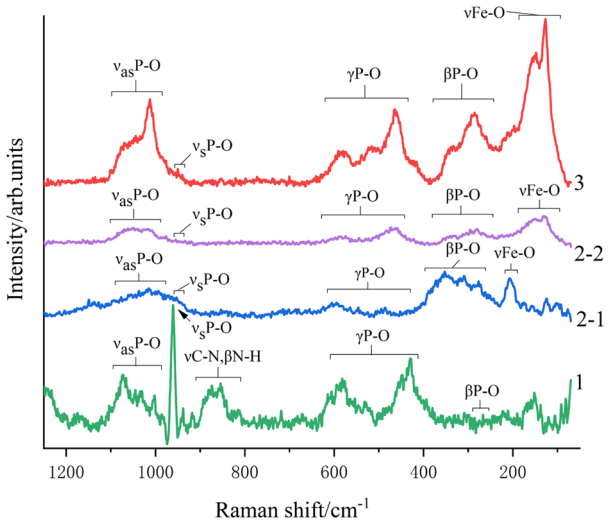

Figure 5. Raman spectra for representative sites in the yellowish-white dentin (1), blue outer layer (2-1) (2-2), and yellowish-brown outer layer (3) of MI-1.

Raman spectra, the antisymmetric stretching vibration of P−O is observed in the 1090−970 cm^{-1} region, while a strong band at around 950 cm^{-1} can be attributed to the P−O symmetric stretching.[33] Furthermore, there are two bands near 500 and 320 cm^{-1} for the four Raman spectra. These bands fit the previously published results for the P−O in-plane and out-of-plane bending, respectively.[34] In spectrum 1, the weak protein features could be observed at the bands of 890, 870, 855, and 815 cm^{-1}. In addition, the vibrations at 206, 148, and 124 cm^{-1} were ascribed to the Fe−O stretching components in the three Raman spectra of the blue outer layer and yellowish-brown outer layer.[35,36]

Based on the above results of peak assignments, spectrum 1 shows characteristic bands that are associated with phosphate and organic matters. Spectra 2-1 and 2-2 correspond to vivianite and metavivianite, respectively.[25] Spectrum 3 corresponds to metavivianite. The bands will overlap each other when santabarbaraite is mixed with metavivianite. Therefore, we are unable to ascertain that santabarbaraite exists in the yellowish-brown outer layer.[31] Determining the presence of santabarbaraite needs to combine with other test methods, such as XPS.

Elemental Mapping by μ-XRF. The blue and yellowish-brown regions disseminate toward the direction of dentin in MI-1 and MI-2. To obtain the chemical composition information of different structures, μ-XRF mapping was carried out on the regions with different structures coexisting shown in Figure 1b,c, and the results are shown in Figures 6 and 7, respectively.

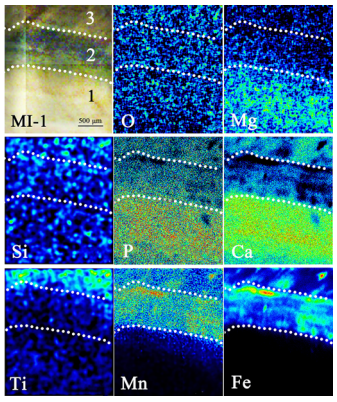

Figure 6. Elemental maps produced by μ-XRF of the yellowish-white dentin (1), blue outer layer (2), and yellowish-brown outer layer (3) in MI-1.

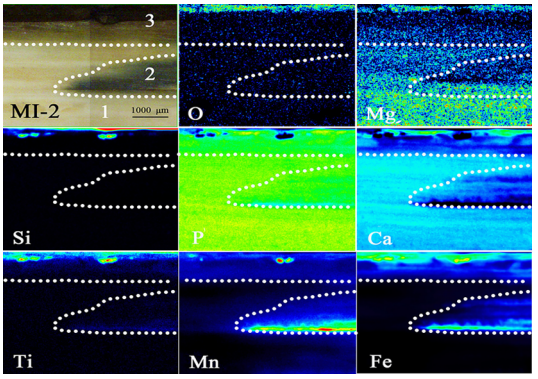

Figure 7. Elemental maps produced by μ-XRF of the yellowish-white dentin (1), blue outer layer (2), and yellowish-brown outer layer (3) in MI-2.

Remarkably, the distribution of oxygen corresponds well to that of silicon in MI-1and MI-2. Based on the XRD and IR results, it is speculated that quartz exists in all three regions of MI-1 and MI-2, and it is more concentrated in the yellowish-brown outer layer.

As can be seen on the mappings, magnesium and phosphorus are mainly distributed in the yellowish-white dentin of MI-1 and MI-2, indicating the distribution characteristics of newberyite ($MgHPO_4{\cdot}3H_2O$).

In the case of calcium, it is also concentrated in the yellowish-white dentin followed by the yellowish-brown outer layer and blue outer layer in that sequence. In conclusion, it is consistent with the distribution characteristics of hydroxyapatite.

In contrast, manganese and iron are centered in the blue and yellowish-brown outer layers, and they also present enrichment along the cracks. It is ascribed to the presence of vivianite and its oxidized products. It is also referred that manganese ions may replace a part of iron ions into the mineral lattice.[37] In addition, manganese and iron show an inverse correlation pattern with calcium.

The environmental titanium is concentrated in the yellowish-brown outer layer and oriented along the cracks in MI-1and MI-2.

XPS. The XPS spectra were collected on the typical dentin and blue and yellowish-brown outer layers of MI-1 shown in Figure 1b, and the results are given in Figure 8. The existence of surface adsorbed oxygen is revealed by the peak at 532.6 eV

https://doi.org/10.1021/acsomega.1c02964
ACS Omega 2021, 6, 22284−22291

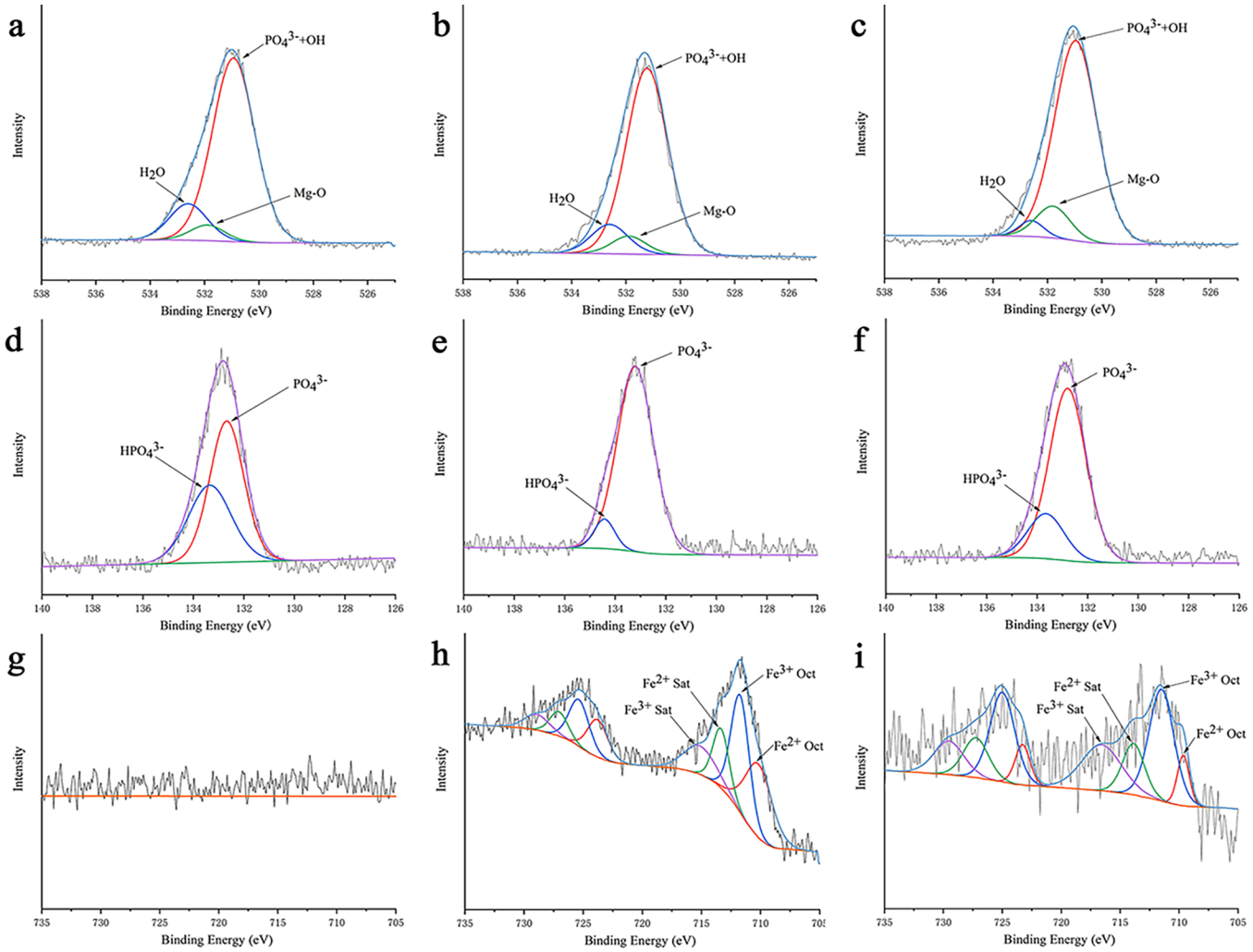

Figure 8. Shirley background-subtracted XPS spectra of the yellowish-white dentin (a,d,g), blue outer layer (b,e,h), and yellowish-brown outer layer (c,f,i) in MI-1.

in the three O (1s) spectra (Figure 8a–c).[38] The peak at 531.9 eV is caused by oxygen in Mg–O, while the peak for phosphate and hydroxyl occurs near 531.1 eV.[38,39] Thus, according to XRD and μ-XRF mapping results, phosphate, newberyite, and surface adsorbed water can be detected in the three different color regions of MI-1.

In the three XPS spectra of P (2p) (Figure 8d–f), the peak ranging from 132.6 to 133.2 eV corresponds to the phosphorus in PO_4^{3-}, and the peak at around 133.3 eV is attributed to the phosphorus in HPO_4^{2-}.[40,41] It demonstrates that phosphorus exists mainly in the form of hydroxyapatite in the three regions of MI-1. It is also inferred that the yellowish-white dentin has the greatest amount of newberyite.

The Fe (2p) spectra were fitted by using the ferrous and ferric multiplet patterns. The results of XPS and peak fitting (Figure 8g–i) show that the yellowish-white dentin almost contains no iron. The peaks at around 711.7 and 710.1 eV are due to the octahedral coordination of Fe^{3+} and Fe^{2+}, respectively. The satellite peaks of Fe^{3+} and Fe^{2+} occur in the range of 715.4–716.6 and 713.4–713.8 eV.[42] The spectra of Fe (2p) indicate the distributions and relative contents of vivianite, metavivianite, and santabarbaraite.

DISCUSSION

Two typical mammoth ivory samples from Yakutsk, Russia, with the yellowish-white dentin and blue and yellowish-brown outer layers from inner to outer were investigated by XRD, vibration spectroscopy, μ-XRF mapping, and XPS. Based on the experimental results, the yellowish-white dentin is mainly composed of hydroxyapatite, newberyite, organic matters, and quartz. The blue outer layer is located below the yellowish-brown outer layer and disseminated toward the dentin. Its main constituent minerals are vivianite and metavivianite, with a small amount of hydroxyapatite, newberyite, quartz, and organic matters. Meanwhile, the yellowish-brown outer layer contains santabarbaraite, metavivianite, hydroxyapatite, newberyite, and quartz.

Vivianite is an easily oxidized hydrated ferrous phosphate mineral. According to the oxidation degree from low to high, its oxidation series can be described as follows: vivianite (monoclinic) → metavivianite (triclinic) → santabarbaraite (amorphous). This process is accompanied by color changes from blue to bluish green then to yellowish brown.[43] In archeology and geology, researchers can judge the sedimentary environment and the formation process of vivianite on the basis of the spatial distribution of vivianite and its oxidized products.[44–51] According to the chemical composition and

https://doi.org/10.1021/acsomega.1c02964
ACS Omega 2021, 6, 22284–22291

oxidized degree of vivianite, some scholars speculated the origin and preservation integrity of works of art.[52,28,53]

The results of μ-XRF mapping and XPS show an apparent iron content in the blue and yellowish-brown outer layers. To further analyze the oxidation degree of vivianite in these two layers, the Fe (2p) peak fitting data are given in Table 1. It

Table 1. Semi-Quantitative Calculation Results of Iron with Different Chemical Valences of the Blue Outer Layer (2) and Yellowish-Brown Outer Layer (3) in MI-1

sites	name	position (eV)	FWHM (eV)	% area
2	Fe^{2+}oct2p3/2	710.45	2.4	34.3
2	Fe^{3+}oct2p3/2	711.81	1.8	36.6
2	Fe^{2+}oct2p1/2	723.82	2.0	13.0
2	Fe^{3+}oct2p1/2	725.45	2.0	16.2
3	Fe^{2+}oct2p3/2	709.63	1.2	9.7
3	Fe^{3+}oct2p3/2	711.50	2.3	44.9
3	Fe^{2+}oct2p1/2	723.23	1.5	9.7
3	Fe^{3+}oct2p1/2	724.99	2.1	35.7
2	total Fe^{2+}			47.3
2	total Fe^{3+}			52.8
3	total Fe^{2+}			19.4
3	total Fe^{3+}			80.6

demonstrates that a part of vivianite has been oxidized in varying degrees. The Fe^{2+} and Fe^{3+} account for 47.3 and 52.8%, respectively, in the blue outer layer, consistent with the result that there are vivianite and metavivianite simultaneously. The values of 19.4% Fe^{2+} and 80.6% Fe^{3+} are detected in the yellowish-brown outer layer. It can be explained by the presence of santabarbaraite and metavivianite in this region. The content difference of Fe^{2+} and Fe^{3+} between the blue and yellowish-brown outer layers reflects the composition distinction of vivianite and its oxidation products. According to their distribution characteristics and relative content differences, we conclude that there was almost no oxidation in the yellowish-white dentin. Meanwhile, the blue outer layer is oxidized to a certain extent, and the yellowish-brown outer layer has the highest oxidation degree. The yellowish-brown outer layer is closer to the external environment so that it is strongly oxidized by the external burial environment.

The experimental results of XRD and μ-XRF mapping show that quartz exists in the three different color regions of mammoth ivory. Also, it is mainly concentrated in the yellowish-brown outer layer. The hydroxyapatite matrix is porous in mammoth ivory, which is beneficial to the infiltration of chemical substances from the surrounding environment.[37] It is speculated that quartz gradually penetrated into mammoth ivory from surrounding rocks or soil. The formation of vivianite requires specific material sources and environmental conditions. The spatial distribution of vivianite shows that the Fe^{2+} in vivianite is provided by the external environment, while the PO_4^{3-} in vivianite originates from mammoth ivory under certain burial effects.[54] In an anoxic frozen soil environment, when Fe^{2+} reaches a specific concentration, it will interact with PO_4^{3-} to form vivianite. With the burial time going on, Fe^{2+} will gradually penetrate into the inside of mammoth ivory and form a gradually thickened vivianite layer. After the formation of the vivianite layer, the burial environment of mammoth ivory, such as the redox conditions, microbial community, temperature, and pressure, may change. Then, vivianite will be oxidized to a series of oxidation products in varying degrees, including dark bluish-green metavivianite, yellowish-brown santabarbaraite, and so on.[55] These processes are also carried out along the direction from outside to inside of mammoth ivory, so there will be a phenomenon that the oxide layers of different colors coexist. The study on the formation and oxidation processes of vivianite can provide some powerful evidence for inferring the burial environment change. With the burial time going on, the blue and yellowish-brown outer layers will further expand toward the center of mammoth ivory. By analyzing the proportion of the blue and yellowish-brown regions in different mammoth tusks under similar conditions, we can compare their relative burial time and preservation integrity.

CONCLUSIONS

The cross section of a typical mammoth ivory sample, unearthed from Yakutsk, Russia, presents the yellow-white, blue, yellowish-brown layers from inside to outside successively. The changes of color in different regions correspond to the distinction of the mineral species and content. The yellowish-white dentin is composed of hydroxyapatite, newberyite, organic matters, and a small amount of quartz. The blue outer layer is located under the yellowish-brown outer layer and extends to the dentin. Its main constituent minerals are vivianite, metavivianite, and a small amount of hydroxyapatite, quartz, newberyite, and organic matters. The yellowish-brown outer layer contains santabarbaraite, metavivianite, hydroxyapatite, newberyite, and quartz.

Vivianite is formed by the interaction of gradually infiltrated Fe^{2+} and original PO_4^{3-} in mammoth ivory. Its series of oxidation products, such as dark bluish-green metavivianite and yellowish-brown santabarbaraite, can form in the later stage. Their formation is related to the changeable burial environment, such as the oxidation−reduction environment or other conditions. The formation of vivianite and its later oxidation process are carried out from the surface to the center of mammoth ivory. Therefore, there is the phenomenon that the oxide layers of different colors coexist. The burial intensity may increase according to the following sequence: the yellowish-white dentin → blue outer layer → yellowish-brown outer layer. The difference in contents of vivianite and its oxidation products reflects the distinction of burial intensity in different color regions of mammoth ivory. By analyzing the proportion of blue and yellowish-brown regions in different mammoth tusks under similar conditions, it can provide evidence for the preservation integrity of mammoth ivory.

AUTHOR INFORMATION

Corresponding Author

Xuemei He − *School of Gemmology, China University of Geosciences, Beijing 100083, China*; Phone: 86-13693203127; Email: Hexuemei3127@126.com

Authors

Mengmeng Shen − *School of Gemmology, China University of Geosciences, Beijing 100083, China*; orcid.org/0000-0001-7688-6993

Zhiyun Lu − *State Key Laboratory of Superhard Materials, College of Physics, Jilin University, Changchun 130012, China*

Yan Xu − *Patent Examination Cooperation (Beijing) Center of The Patent Office, CNIPA, Beijing 100160, China*

Complete contact information is available at:

https://doi.org/10.1021/acsomega.1c02964
ACS Omega 2021, 6, 22284−22291

https://pubs.acs.org/10.1021/acsomega.1c02964

Notes

The authors declare no competing financial interest.

■ ACKNOWLEDGMENTS

The authors thank Wannian Jixiang (Beijing) Jewelry Co., Ltd. for providing us with the research samples. This research was funded by the project of "Geology of mineral resources in China" from China Geological Survey (Grant No. DD20160346, DD20190379).

■ REFERENCES

(1) Heckel, C.; Müller, K.; White, R.; Wolf, S.; Conard, N. J.; Normand, C.; Floss, H.; Reiche, I. F-content variation in mammoth ivory from Aurignacian contexts: Preservation, alteration, and implications for ivory-procurement strategies. *Quat. Int.* **2016**, *403*, 40−50.

(2) Reiche, I.; Heckel, C.; Müller, K.; Jöris, O.; Matthies, T.; Conard, N. J.; Floss, H.; White, R. Combined Non-invasive PIXE/PIGE Analyses of Mammoth Ivory from Aurignacian Archaeological Sites. *Angew. Chem., Int. Ed.* **2018**, *57*, 7428−7432.

(3) Borgia, V. The mammoth cycle. Hunting with ivory spear-points in the Gravettian site of Pavlov I (Czech Republic). *Quat. Int.* **2019**, *510*, 52−64.

(4) Burragato, F.; Materazzi, S.; Curini, R.; Ricci, G. New forensic tool for the identification of elephant or mammoth ivory. *Forensic Sci. Int.* **1998**, *96*, 189−196.

(5) Heckel, C. E.; Wolf, S. Ivory debitage by fracture in the Aurignacian: experimental and archaeological examples. *J. Archaeol. Sci.* **2014**, *42*, 1−14.

(6) Steguweit, L. Rotten ivory as raw material source in European Upper Palaeolithic. *Quat. Int.* **2015**, *361*, 313−318.

(7) Wolf, S.; Heckel, C. Ivory Ornaments of the Aurignacian in Western Europe: Case studies from France and Germany Éléments de parure en ivoire de l'Aurignacien d'Europe occidentale : études de cas en France et en Allemagne. *L'Anthropologie* **2018**, *122*, 348−373.

(8) Wygal, B. T.; Krasinski, K. E.; Holmes, C. E.; Crass, B. A. Holzman South: A Late Pleistocene Archaeological Site along Shaw Creek, Tanana Valley, Interior Alaska. *PaleoAmerica* **2018**, *4*, 90−93.

(9) Vercoutère, C.; Müller, K.; Chiotti, L.; Nespoulet, R.; Staude, A.; Riesemeier, H.; Reiche, I. Rectangular Beads from the Final Gravettian Level of the Abri Pataud: Raw Material Identification and its Archaeological Implications. *ArcheoSciences* **2011**, *35*, 259−271.

(10) Conard, N. J. Palaeolithic ivory sculptures from southwestern Germany and the origins of figurative art. *Nature* **2003**, *426*, 830−832.

(11) Saunders-Jeffrey, J.; Haynes, C. V.; Dennis, S.; Agogino-George, A. A Mammoth-Ivory Semifabricate from Blackwater Locality No. 1, New Mexico. *Am. Antiq.* **1990**, *55*, 112−119.

(12) Lázničková-Galetová, M. The phenomenon of Gravettian necklaces − Mammoth ivory necklaces from Dolní Věstonice I (Moravia, Czech Republic). *Quat. Int.* **2015**, *359-360*, 229−239.

(13) Pitulkoa, V. V.; Pavlovab, E. Y.; Nikolskiyc, P. A. Mammoth ivory technologies in the Upper Palaeolithic: a case study based on the materials from Yana RHS, Northern Yana-Indighirka lowland, Arctic Siberia. *World Archaeol.* **2015**, *47*, 333−389.

(14) Schott, G. D. Engraved hexagons on an Ice Age ivory: a neurological perspective on an anthropological debate. *J. Neurol., Neurosurg. Psychiatry* **2014**, *85*, 1174−1176.

(15) Ngatia, J. N.; Lan, T. M.; Ma, Y.; Dinh, T. D.; Wang, Z.; Dahmer, T. D.; Xu, Y. C. Distinguishing extant elephants ivory from mammoth ivory using a short sequence of cytochrome b gene. *Sci. Rep.* **2019**, *9*, 2389−2400.

(16) Heckel, C. Physical characteristics of mammoth ivory and their implications for ivory work in the Upper Paleolithic. *Mitt. der Gesellschaft Urgeschichte* **2009**, *18*, 71−91.

(17) Pitulko, V. V.; Nikolskiy, P. A. The extinction of the woolly mammoth and the archaeological record in Northeastern Asia. *World Archaeol.* **2012**, *44*, 21−42.

(18) Freund, A.; Eggert, G.; Kutzke, H.; Barbier, B. On the occurrence of magnesium phosphates on ivory. *Stud. Conserv.* **2002**, *47*, 155−160.

(19) Cartier, L. E.; Krzemnicki, M. S.; Gysi, M.; Lendvay, B.; Morf, N. V. A Case Study of Ivory Species Identification Using a Combination of Morphological, Gemmological and Genetic Methods. *J. Gemmol.* **2020**, *37*, 282−297.

(20) Matienzo, L. J.; Snow, C. E. The chemical effects of hydrochloric acid and organic solvents on the surface of ivory. *Stud. Conserv.* **1986**, *31*, 133−139.

(21) Edwards, H. G. M.; Jorge Villar, S. E.; Nik Hassan, N. F.; Arya, N.; O'Connor, S.; Charlton, D. M. Ancient biodeterioration: an FT-Raman spectroscopic study of mammoth and elephant ivory. *Anal. Bioanal. Chem.* **2005**, *383*, 713−720.

(22) Yin, Z.-w.; Luo, Q.-f.; Zheng, C.; Bao, D.-q.; Li, X.-l.; Li, Y.-l.; Chen, Q.-l. The spectrum characteristic analysis of mammoth ivory. *Spectrosc. Spectral Anal.* **2013**, *33*, 2338−2342.

(23) Allegrini, S., Jr.; Rumpel, E.; Kauschke, E.; Fanghänel, J.; König, B., Jr. Hydroxyapatite grafting promotes new bone formation and osseointegration of smooth titanium implants. *Ann. Anat. - Anat. Anz.* **2006**, *188*, 143−151.

(24) El-Anwar, A.; Esmat, A. Lithologic characterization of the phosphorite-bearing Duwi Formation (Campanian), South Esna, West Nile Valley, Egypt. *Carbonates Evaporites* **2019**, *34*, 793−805.

(25) Čermáková, Z.; Švarcová, S.; Hradilová, J.; Bezdička, P.; Lančok, A.; Vašutová, V.; Blažek, J.; Hradil, D. Temperature-related degradation and colour changes of historic paintings containing vivianite. *Spectrochim. Acta A* **2015**, *140*, 101−110.

(26) Madsen, H. E. L. Morphology and Optical Properties of Precipitated Vivianite, $Fe_3(PO_4)_2{\cdot}8H_2O$. *Cryst. Res. Technol.* **2020**, *55*, 1900226.

(27) Henderson, G. S.; Black, P. M.; Rodgers, K. A.; Rankin, P. C. New data on New Zealand vivianite and metavivianite. *N. Z. J. Geol. Geophys.* **2012**, *27*, 367−378.

(28) Bratu, I.; Nemeş, O. F.; Mărunţoiu, V. C.; Kácso, I.; Vlasin, D. G. Characterization of a Jesus Pantocrator Wooden Icon from Eighteen Century by Differential Scanning Calorimetry and Infrared and X-ray Fluorescence Spectroscopies. *Anal. Lett.* **2019**, *52*, 45−53.

(29) Ogorodova, L.; Vigasina, M.; Mel'chakova, L.; Rusakov, V.; Dosova, K.; Ksenofontov, D.; Bryzgalov, I. Enthalpy of formation of natural hydrous iron phosphate: Vivianite. *J. Chem. Thermodyn.* **2017**, *110*, 193−200.

(30) Chukanov, N. V.; Scholz, R. S.; Aksenov, S. M.; Rastsvetaeva, R. K.; Pekov, I. V.; Belakovskiy, D. I.; Krambrock, K.; Paniago, R. M.; Righi, A.; Martins, R. F. Metavivianite, $Fe^{2+}Fe^{3+}{}_2(PO_4)_2(OH)_2{\cdot}6H_2O$: new data and formula revision. *Mineral. Mag.* **2012**, *76*, 725−741.

(31) Čermáková, Z.; Hradilová, J.; Jehlička, J.; Osterrothová, K.; Massanek, A.; Bezdička, P.; Hradil, D. Identification of Vivianite in Painted Works of Art and Its Significance for Provenance and Authorship Studies. *Archaeometry* **2014**, *56*, 148−167.

(32) Fagel, N.; Alleman, L. Y.; Granina, L.; Hatert, F.; Thamo-Bozso, E.; Cloots, R.; André, L. Vivianite formation and distribution in Lake Baikal sediments. *Global Planet. Change* **2005**, *46*, 315−336.

(33) Kloprogge, J. T.; Visser, D.; Martens, W. N.; Duong, L. V.; Frost, R. L. Identification by RAMAN Microscopy of magnesian vivianite formed from Fe^{2+}, Mg, Mn^{2+} and $PO_4{}^{3-}$ in a Roman camp near fort Vechten, Utrecht, The Netherlands. *Neth. J. Geosci.* **2003**, *82*, 209−214.

(34) Chua, L.; Maynard-Casely, H. E.; Thomas, P. S.; Head, K.; Stuart, B. H. Characterisation of blue pigments from ceremonial objects of the Southern Highlands in Papua New Guinea using vibrational spectroscopy and X-ray diffraction. *Vib. Spectrosc.* **2016**, *85*, 43−47.

(35) Frost, R. L.; Weier, M. L.; Martens, W.; Kloprogge, J. T.; Ding, Z. Dehydration of synthetic and natural vivianite. *Thermochim. Acta* **2003**, *401*, 121−130.

(36) Frost, R. L.; Martens, W.; Williams, P. A.; Kloprogge, J. T. Raman and infrared spectroscopic study of the vivianite-group phosphates vivianite, baricite and bobierrite. *Mineral. Mag.* **2002**, *66*, 1063−1073.
(37) Skinner, H. C. W. Biominerals. *Mineral. Mag.* **2005**, *69*, 621−641.
(38) Pratt, A. R. Vivianite auto-oxidation. *Phys. Chem. Miner.* **1997**, *25*, 24−27.
(39) Manciu, F. S.; Govani, J. R.; Durrer, W. G.; Reza, L.; Pinales, L. A. Inhibition of urinary calculi—a spectroscopic study. *J. Raman Spectrosc.* **2009**, *40*, 861−865.
(40) Xie, F.; Wu, F.; Liu, G.; Mu, Y.; Feng, C.; Wang, H.; Giesy, J. P. Removal of phosphate from eutrophic lakes through adsorption by in situ formation of magnesium hydroxide from diatomite. *Environ. Sci. Technol.* **2014**, *48*, 582−590.
(41) Zhang, B.; Wang, L.; Li, Y. Fractionation and identification of iron-phosphorus compounds in sewage sludge. *Chemosphere* **2019**, *223*, 250−256.
(42) Lu, Z.; He, X.; Lin, C.; Liang, L.; Jin, X.; Guo, Q. Color and genesis of californite from Pakistan: insights from μ-XRF mapping, optical spectra and X-ray photoelectron spectroscopy. *Sci. Rep.* **2020**, *10*, 605−616.
(43) Rothe, M.; Kleeberg, A.; Hupfer, M. The occurrence, identification and environmental relevance of vivianite in waterlogged soils and aquatic sediments. *Earth-Sci. Rev.* **2016**, *158*, 51−64.
(44) Huang, F.; Xu, C. Q.; Jin, Z. M.; Hu, M. L.; Cai, H. Perfect vivianite crystals excavated from a highly sealed ancient tumulus in Jing'an County, Jiangxi Province, China. *Archaeol. Prospect.* **2019**, *27*, 63−70.
(45) Maritan, L.; Casas, L.; Crespi, A.; Gravagna, E.; Rius, J.; Vallcorba, O.; Usai, D. Synchrotron tts-μXRD identification of secondary phases in ancient ceramics. *Heritage Sci.* **2018**, *361*, 313−318.
(46) Lucrezia, C.; Julien, M.; Monica, A.; Frederic, S.; Pilar, J.; Edith, J. Use of Bacteria To Stabilize Archaeological Iron. *Appl. Environ. Microbiol.* **2017**, *83*, 759−772.
(47) Papageorgopoulou, C.; Link, K.; Rühli, F. J. Histology of a Woolly Mammoth (Mammuthus primigenius) Preserved in Permafrost, Yamal Peninsula, Northwest Siberia. *Anat. Rec.* **2015**, *298*, 1059−1071.
(48) Taylor, G.; Hefford, R. J. W.; Birley, A.; Huntley, J. P. Identifying the "blue substance" at the Roman site of Vindolanda, Northumberland. *J. Archaeol. Sci.* **2019**, *24*, 582−587.
(49) Thali, M. J.; Lux, B.; Lösch, S.; Rösing, F. W.; Hürlimann, J.; Feer, P.; Dirnhofer, R.; Königsdorfer, U.; Zollinger, U. "Brienzi" − The blue Vivianite man of Switzerland: Time since death estimation of an adipocere body. *Forensic Sci. Int.* **2011**, *211*, 34−40.
(50) Zangarini, S.; Trombino, L.; Cattaneo, C. Micromorphological and ultramicroscopic aspects of buried remains: Time-dependent markers of decomposition and permanence in soil in experimental burial. *Forensic Sci. Int.* **2016**, *263*, 74−82.
(51) Grizelj, A.; Bakrač, K.; Horvat, M.; Avanić, R.; Hećimović, I. Occurrence of vivianite in alluvial Quaternary sediments in the area of Sesvete (Zagreb, Croatia). *Geol. Croat.* **2017**, *70*, 41−52.
(52) Figueiredo, M. O.; Silva, T. P.; Veiga, J. P. The blue of iron in mineral pigments: a Fe K-edge XANES study of vivianite. *Appl. Phys. A* **2010**, *99*, 357−361.
(53) Scott, D. A.; Eggert, G. The vicissitudes of vivianite as pigment and corrosion product. *Stud. Conserv.* **2013**, *52*, 3−13.
(54) McGowan, G.; Prangnell, J. The significance of vivianite in archaeological settings. *Geoarchaeology* **2006**, *21*, 93−111.
(55) Hanzel, D.; Meisel, W.; Hanzel, D.; Gütlich, P. Conversion electron Mössbauer study of vacuum and thermally treated vivianite. *Hyperfine Interact.* **1990**, *57*, 2201−2207.

https://doi.org/10.1021/acsomega.1c02964
ACS Omega 2021, 6, 22284−22291